Impuls- und Vernetzungsfonds

Zwischenbericht 2016

Förderprogramm:	**Virtuelle Institute**
Impulsfonds-Projektnummer:	VH-VI-403
Projekttitel:	In-Situ Nano-Imaging of Biological and Chemical Processes
Federführende/r Wissenschaftler/in	Christian Schroer
Berichtszeitraum (Förderungszeitraum)	01.01.2016 – 31.12.2016

Sachbericht

1 Fortschritt des im Antrag beschriebenen Arbeitsprogramms

In the framework of this VI, the following sub-projects have been addressed during the year 2016:

- 1.1 Cardiomyocytes and cadiac muscle tissue studied by scanning diffraction and holography (AG Salditt)
- 1.2 Combining microfluidics and x-rays (AG Köster)
- 1.3 Microfluidic sample chambers for studies of synaptic vesicles (AG Salditt & AG Köster)
- 1.4 Cellular imaging using x-rays (AG Köster & AG Schroer)
- 1.5 Ultrastructure and chemistry of melanosomes in view of the development of glaucoma (AG Rosenhahn)
- 1.6 X-ray nanoprobe analysis of diatom adhesives (AG Rosenhahn)
- 1.7 Design of in situ cell for ptychography and time-resolved imaging of catalyst ageing during the sintering process (AG Grunwaldt & AG Schroer)
- 1.8 Towards 3D imaging of heterogeneous catalysts: structural changes and reaction gradients observed by in situ tomography (AG Grunwaldt)
- 1.9 Microfluidic reactor for studies on early stage kinetics and formation of metallic nanoparticles, colloids and precipitates (AG Grunwaldt)
- 1.10 Multimodal scanning microscopy with diffraction and fluorescence contrast (AG Schroer)
- 1.11 Instrumentation, dissemination of methods and user experiments on in-situ chemical and biological processes (AG Salditt, AG Schroer)

These sub-projects are described in more detail below.

1.1 Cardiomyocytes and cadiac muscle tissue studied by scanning diffraction and holography (AG Salditt)

The goal of the experiments in 2016 was to illucidate the formation of sarcomeric structure in single cardiac muscle cells by means of scanning nano-diffraction using the nanofocus instrument GINIX at beamline P10 at PETRA III. The studies focused on hiPS cells (human induced pluripotent stem cells) derived into cardiomyocytes in addition to previously employed neonatal rat cardiomyocytes [1] due to their myofilaments being more strongly developed. Scanning SAXS data were recorded on freeze-dried and vitrified (or cryo-protected) samples as well as alive preparations. Experiments on living iPS cell cultures were prepared by pre-culturing in the S2 biological laboratory at the beamline one week in advance to provide enough time for cell growth and structural development. To this end, we have streamlined our wet chamber setup based on two sandwiched silicon nitride membranes (Silson Ltd., UK) and obtained first promising x-ray darkfield images of living cells. Our experiments were complemented by model systems based on crosslinked actin assemblies measured in a vitrified state. α-actinin and fascin were used as actin cross-linkers due to ability to form (loosly or thightly bound) parallel bundels.

For all experiments at beamline P10, the photon energy was set to 13.8 keV and the Eiger X 4M detector (2070×2167 pixels, 75 µm pixel size) was used for data acquisition at 5.12 m distance from the focus. Scanning SAXS measurements on freeze-dried cells where routinely recorded at a resolution well below 1 µm. The sample, freeze-dried cells adherent to a 1 mm thick SiRN (silicon-enriched nitride) window was hereby scanned through the focus of the KB beam (beam size approx. 300 nm × 300 nm, KB entrance slits tuned to 0.2 mm × 0.2 mm) and cryo-protected using a cold nitrogen gas stream (cryostream). In some cases, ice formation could not easily be avoided when inserting the sample into the cold gas stream, and resulting artifacts have to be removed in a subsequent analysis.

In contrast, actin networks crosslinked by fascin and α-actinin deposited on SiRN windows were vitrified and mounted with some effort directly into the cryostream for experiments. The protein network can clearly be depicted in both cases, see Fig. 1b. While scattering is dominated by streak-like diffraction patterns that decay smoothly along q_r (reciprocal wave vector), in some cases the scattering is modulated as expected due to the bundling of the actin-binding proteins. However, it has to be further investigated, wether this effect stems from the actin network or smaller ice crystal domains and/or how well the actin bundle period can be mapped along the entire scan.

In addition, we have performed first scanning SAXS measurements on alive cells. To this aim, cells were prepared one week in advance at the biology laboratory of the endstation P10. Cells were deposited on SiRN (silicon-enriched nitride) membranes and allowed

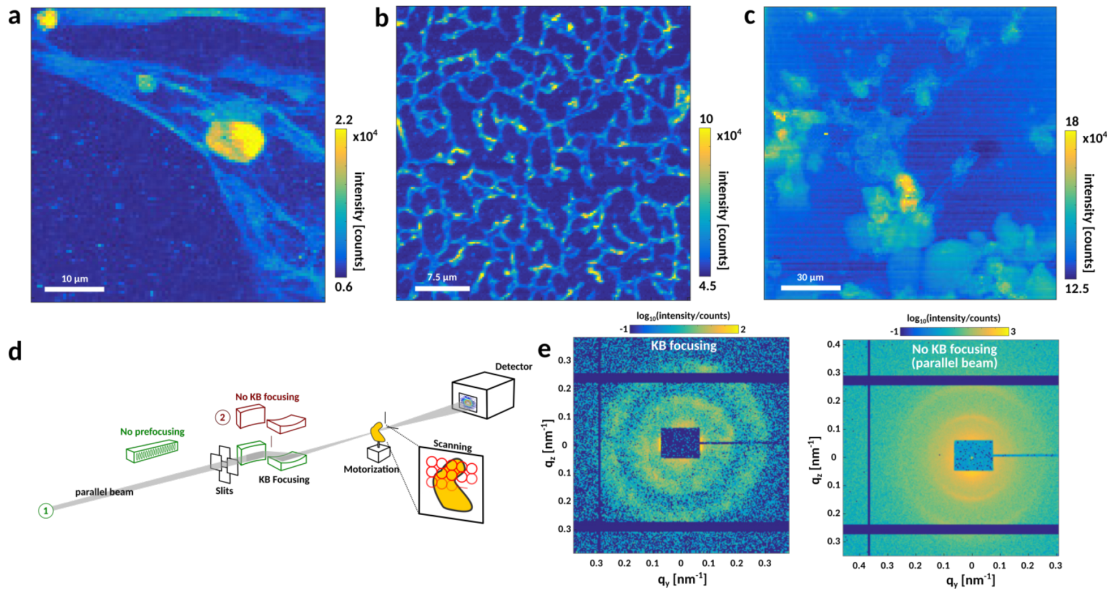

Figure 1: Examples of scanning SAXS data of a) Freeze-dried and cryo-protected hiPS cells (101×101 scan points, 0.5 µm step size), b) actin network crosslinked with α-actinin (161×161 scan points, 0.25 µm step size), and c) alive hiPS cells in nutrition medium (151×151 scan points, 1 µm step size). d) Two configurations of the experimental setup. In case of (1, green), KB focusing was used to reach a focal spot size of approx. 300 nm × 300 nm. After removal of the KB mirrors, the primary beam was used, collimated to 20 µm × 20 µm. e) Scattering patterns on heart muscle tissue (longitudinal cut, 30 µm slice thickness) with and without KB focusing. When KB focusing is used, scattering maxima are broadened due to the divergence of the beam, as compared to a parallel beam experiment.

to grow for about one week. Directly prior to the experiment, the cells were contained between two SiRN windows and carefully sealed by polymer clips (Silson Inc., UK). With further improvements in our workflow, we could optimize sample transfer and almost rule out leakage, hereby making x-ray studies on alive preparations feasible that also bears great potential for complementary real-time x-ray imaging studies. Equipment necessary for handling of S2 samples at the beamline was kindly provided by Dr. Stellamans.

Cardiac muscle cells are clearly depicted in the scanning SAXS image (darkfield contrast) within their natural aqueous environment, see Fig. 1c. So far, while cells can be clearly distinguished from solution background, scattering seems nonetheless to be primarily isotropic with only slight contributions minor cellular structure.

Lastly, we aimed at linking nanofocus scanning experiments to classical SAXS studies on cardiac muscle by mapping out the sarcomeric structure with and without KB focusing (primary beam, beam size approx. 20 µm × 20 µm). This was done for living iPS cell

cultures as well as cardiac muscle tissue (longitudinal and transversal cuts). In the case of heart muscle, we could observe the typical diffraction peaks from the sarcomere. In an analogous manner, the same diffraction spots were observed without KB focusing with a parallel beam, however, at higher signal to noise ratio and significantly less broadening due to the larger divergence of the KB beam, see Fig. 1e. Data analysis of all experimental parts is ongoing.

1.2 Combining microfluidics and x-rays (AG Köster)

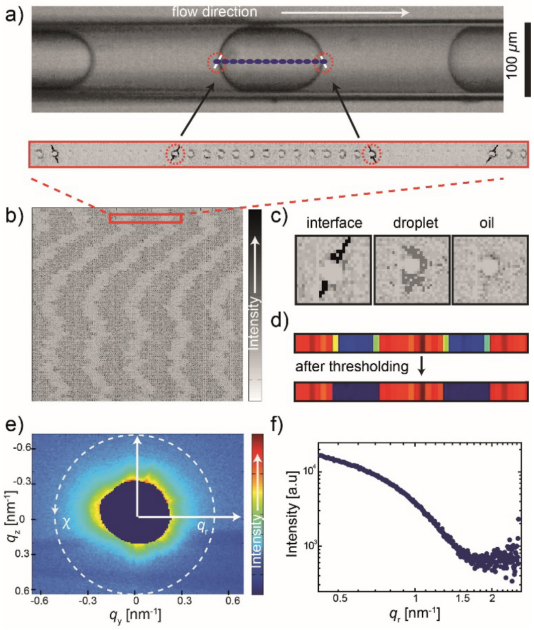

Figure 2: a) Micrograph of a capillary segment from the composite device in which the droplets are flowing by the X-ray beam. The blue dots denote representative measurement positions. A corresponding composite image of the resulting scattering patterns is shown below. b) Composite images from approximately 250 droplets flowing by the beam arranged in rows. The transition between drops and the continuous oil phase is clearly visible. c) Typical 2D-scattering patterns of (left to right) the interface between oil and aqueous phase, droplet, and oil. d) X-ray dark field composite image of few droplets flowing by the beam. Post-processing of the data involves thresholding. e) Representative averaged scattering pattern from within the droplets with mask blocking the primary beam. f) 1D-scattering profile after integrating the signal from (e). (From Ref. [3]).

We worked further on developing different ways to produce x-ray compatible microfluidic devices. A very versatile device is shown in Figure 2; it consists of a PDMS structure to produce microfluidic drops and a glass capillary which is well suited for the x-ray measurements. These devices are easy to produce and we have already passed this knowledge on to collaborating groups. The key here are fast detectors that can capture multiple exposures per flowing droplet and an automated analysis algorithm.

Further we have developed devices made from COC and are just now working on a corresponding publication in order to make this information available to the community.

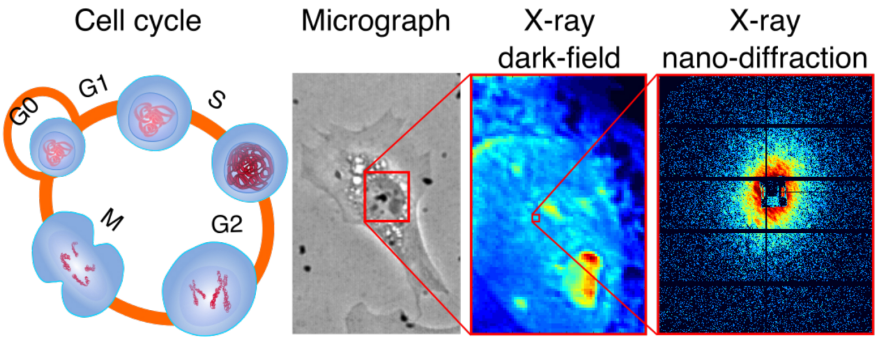

Figure 3: Time and space resolved cellular imaging by combining visible light microscopy with scanning SAXS (from Ref. [4]).

1.3 Microfluidic sample chambers for studies of synaptic vesicles (AG Salditt & AG Köster)

We have performed proof-of-concept experiments at PETRA III/P10 and at ID02/ESRF on suitable sample environments for high throughput structural analysis of entire synaptic organelles. Structural parameters are size, density, and protein localisation. Beyond structure, we also plan to probe controlled interactions of organelles and proteins. Towards these goals, we have combined SAXS with microfluidic devices.

1.4 Cellular imaging using x-rays (AG Köster & AG Schroer)

We intensified our effort in developing innovative ideas for cellular imaging using x-rays. After focusing mostly on the cytoskeleton in the past (see, e. g., Ref. [5]), we now added DNA in cell nuclei to our systems of interest. By combining visible light microscopy with scanning SAXS we were able to follow the cell division cycle in mammalian cells. We recorded movies of cells grown on Si_3N_4 substrates in order to monitor their division behaviour. Samples were then chemically fixed, plunge-frozen and freeze-dried. The experiments were performed at the GINIX end station of the P10 beamline at PETRA III. Scanning small angle x-ray scattering (SAXS) was performed and different regions within the nuclei of the cells were identified, corresponding to different degrees of compaction. We were also able to relate different relative time points in the division cycles to differently packed DNA.

At the end of 2016 we performed follow up experiments at P10 combining scanning SAXS with holography and we hope that from these data we will derive the electron density contrast directly thus being able quantify the degree of compaction in a more precise way than previously.

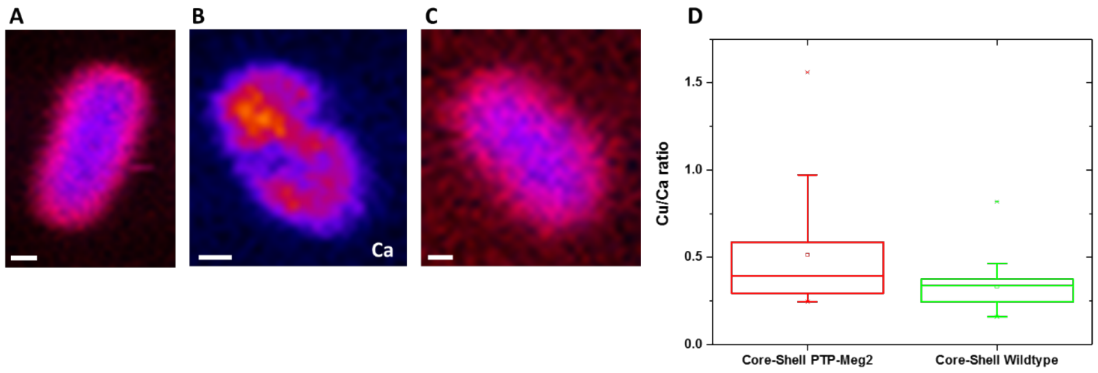

Figure 4: X-ray fluorescence measurements of melanosomes of 28 weeks old mice. The scale bar is 100 nm. A) Core-Shell PTP-Meg2 melanosome (Ca signal shown in blue, Cu signal shown in red). B: Ca signal of a deformed melanosome of PTP-Meg2 mouse. C: Core-Shell wildtype melanosome. D: Comparison of the Ca/Cu ratio of melanosomes which occur to have the core-shell form, PTP-Meg2 is shown in red, wildtype shown in green.

1.5 Ultrastructure and chemistry of melanosomes in view of the development of glaucoma (AG Rosenhahn)

Melanosomes are intracellular membrane-bound organelles which produce and store melanin [35]. In the beginning of the Virtual Institute, melanosomes from the DBA2J glaucoma prototype mutant from the Jackson-Laboratory in Maine was compared against wild type species. In the past years we extended the range of mutants by a cooperation with biologists from the Ruhr-University Bochum (Dr. Reinhardt, Prof. Faissner) towards the PTP-Meg2 deficient mouse line [36]. As the eye pressure which is a symptom for glaucoma starts to increase after 9 weeks we chose two different ages of mice for comparison [36].

We tested if the recently proven casing model which predicts that melanosomes consist of a pheomelanin core surrounded by a eumelanin shell is also valid for PTP-Meg2 mutant [37, 38]. We used cryogenic in-situ sample environments to investigate samples without disturbing artefacts due to sample drying. In both ages we found a core-shell structure for most of the melanosomes in both wildtype and glaucomatous mice. This means that the core-shell structure is established in an early developmental phase and remains virtually unchanged at higher ages. While in young mice and the 28 week old wild type mice the only shape of melanosomes found was roundish, there was a higher variety of melanosome shapes in 28 week old PTP-Meg2 mice. In these old mutants, only 50-60 % of the investigated cells were ellipsoid and showed the core-shell structure. A high number was round or had a very low copper content. Conspicuously 20 % of the melanosomes looked deformed with a broken cell wall, which could not be seen in the wildtype mice (see Fig. 4B). The loss of integrity of the melanosome structure could

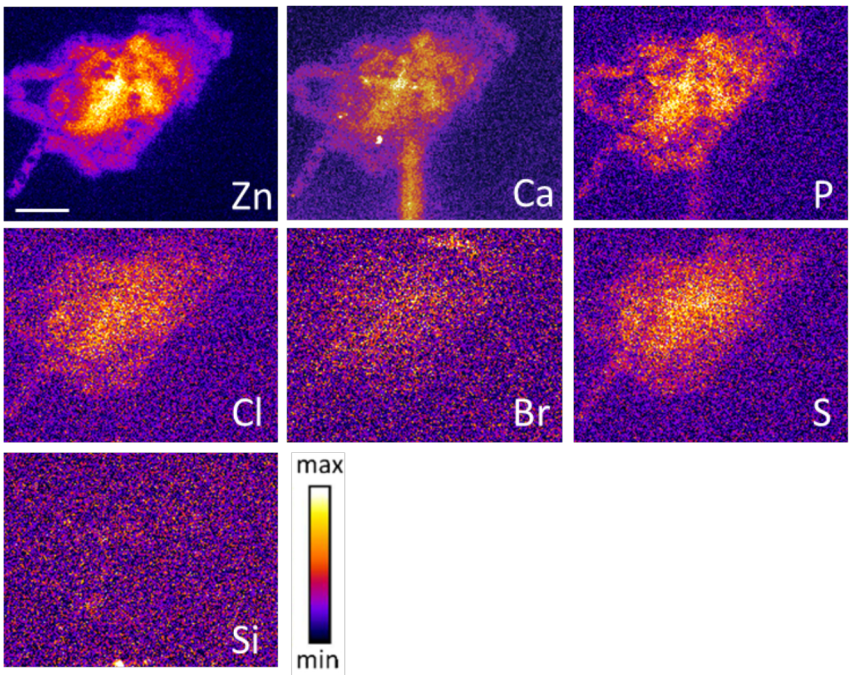

Figure 5: Fluorescence signal of the EPS of the diatom *N. perminuta* after removal of the alga. The scale bar is 1 µm.

cause a liberation of cytotoxic indols that might lead to cell debris to clog the trabecular meshwork in the eye and consequently lead to enhanced eye pressure. Besides a different shape we found an enhanced copper content in the melanosomes of PTP-Meg2 mice. While in the young mice the copper content was the same in both wildtype and PTP-Meg2 mice, in the old mice the copper concentration was significantly higher in the mutant (see Fig. 4D). This indicates that copper enrichment in the glaucomatous mice only occurs after a relatively long time and seems to be part of the growth process of mice that suffer from glaucoma.

1.6 X-ray nanoprobe analysis of diatom adhesives (AG Rosenhahn)

Based on our first experiments on the composition of the shell of the diatom *Navicula perminuta* described in the previous reports, our focus in the past year was on metals that occur in the extracellular polymeric substance (EPS) of the diatom. The alga is a marine biofilm forming organism and is frequently appearing at ship hulls and prevalent on most antifouling coatings [39, 40]. After settling the algae on hydrophobic or hydrophilic Kapton foils we could remove the organisms by a water jet completely from the surfaces without destroying the EPS. As the algal shell consists of calcium, sulfur, zinc, bromine, strontium and mainly of silicon, we could use the silicon signal as a marker for non-removed algae. The regions where algae were grown were marked before

removal to be able to quickly access the regions of interest. The EPS has some elements in common with the algae but has a high concentration of zinc (see Fig. 5). This zinc signal could be spatially correlated with calcium, phosphorus, chlorine, bromine, and sulfur. In general, the number of settled diatoms was higher on the hydrophobic than on the hydrophilic surfaces. The composition of the EPS differed on both surfaces as the EPS on the hydrophilic surface contained more zinc. We currently try to understand if the higher Zn content is linked to a different attachment strength or if it is connected to a different organic constituent of the adhesive that establishes the contact to the interface.

1.7 Design of in situ cell for ptychography and time-resolved imaging of catalyst ageing during the sintering process (AG Grunwaldt & AG Schroer)

To study catalysts at the nanometer length scale, special in situ cells were developed in collaboration with Ass. Prof. Dr. C. D. Damsgaard at the Technical University of Denmark (DTU). These cells offer the possibility to characterize congruent areas of a sample by complementary X-ray and electron microscopy. Apart from the relatively big cell presented in the Mid-Term review of VI-VI-403 in 2014, another smaller cell was developed. Both cells can be applied for in situ hard X-ray ptychography and are capable of studying samples in a controlled gas environment and at elevated temperatures. Since the samples are placed on TEM heating chips, they can be studied by complementary TEM before and after the in situ ptychography experiment. Both cells are available for 2D imaging, but they differ from each other by their dimensions and gas volumes, as well as the applicability for complementary fluorescence contrast, which is only possible for the smaller cell. Both cells are presented in Figure 6. The bigger cell presented in Figure 6b) was intensively used to examine the coarsening of nanoporous gold [6, 7] and the stability of a core@shell particle [8], while the smaller one (c. f. Figure 6a) was only used for preliminary tests so far, but has been shown to allow complementary fluorescence contrast.

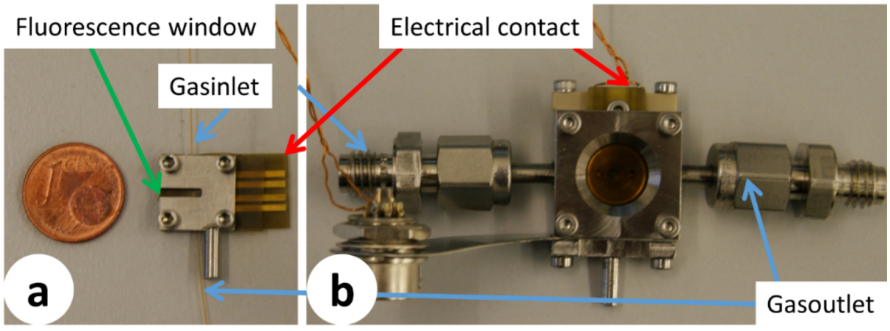

Figure 6: In situ cells for 2D hard X-ray ptychography next to each other. a) Smaller cell, derived from an improvement of the first cell which is presented in b).

1.8 Towards 3D imaging of heterogeneous catalysts: structural changes and reaction gradients observed by in situ tomography (AG Grunwaldt)

Non-destructive 3D imaging of catalysts can be realized by X-ray Computed Tomography (CT). Scanning techniques can be combined with numerous acquisition modes, including X-ray Fluorescence (XRF) and XRD for example, in parallel to absorption contrast. In situ Scanning Transmission X-ray Tomography (STXM) on a core@shell catalyst for DME production was performed in collaboration with Diamond I18 beamline, in combination with microfocus XRD-CT and XRF-CT, with spatial resolution on the order of 2 µm. The catalyst was studied in the freshly prepared state, and subsequently under calcination, reduction and reaction conditions. While the core was visible by both μ-XRF-CT and μ-XRD-CT, the zeolite shell could only be examined with μ-XRD-CT, which also offered information about the crystalline phases of copper and zinc within the core. The study revealed that under reducing atmosphere, copper species showing different oxidation states (Cu^+ and Cu^0) were observed, rather than a homogeneous metallic copper phase. In particular, a gradient of Cu^+ at the core-shell interface was observed. Under reaction atmosphere, the structure slightly changed again, indicating the existence of both metallic and partially-oxidized copper phases, which is in line with current debates in literature [41, 42, 43]. Finally, μ-XRF-CT revealed that ZnO within the core was relatively stable and well dispersed under all conditions, while the reduced and active catalyst revealed high dispersion of the copper phases, again in agreement with long-standing literature on this topic. The differences obtained by XRD/XRF-μ-STXM are presented in Figure 7. These observations would not have been possible without tomographic in situ studies offering 3D spatial resolution. This highlights the importance of such methods for the characterization of heterogeneous catalysts, particularly those with complex or hierarchical structures.

Furthermore, design of a next generation in situ cell for further tomography studies is continuing, particularly to address the study of reaction gradients and catalyst ageing processes, e. g., during partial oxidation of methane. The cell was used to study the behavior of bismuth molybdenum oxides, which are applied in the selective oxidation of propene to acrolein. The cell body during its application at the beamline as well as the scheme of the optimized cell are presented in Figure 8.

1.9 Microfluidic reactor for studies on early stage kinetics and formation of metallic nanoparticles, colloids and precipitates (AG Grunwaldt)

Microfluidic devices which allow turbulent flows can be used to study reaction kinetics and mechanisms by following the progress of a reaction in a spatially resolved way. Here, the reaction kinetics and mechanisms of gold nanoparticle (Au NP) formation [44, 45] by the chemical reduction method were examined. A microfluidic setup [9]

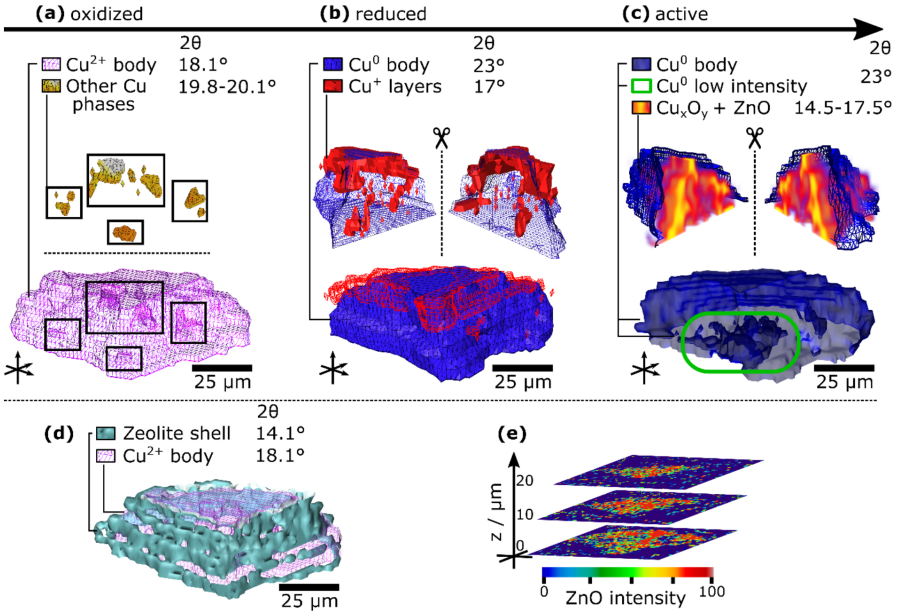

Figure 7: Life cycle of the $Cu/ZnO/Al_2O_3$@ZSM-5 core@shell particle under in situ conditions, with XRD-CT renderings of: (a) CuO body with partially reduced fractions under O_2 at 400 °C; (b) Cu^0 body with outer layer of stable Cu_2O under H_2 at 250 °C; (c) Cu^0 body with large areas of mixed Cu_xO_y oxidation states and ZnO; (d) core and shell occupying distinct 3D space (oxidizing conditions); (e) ZnO intensity maps ($2\Theta = 16.9°$) for several slices under reducing conditions.

was built to study the early stages (down to milliseconds) of fast reduction reactions using strong reducing agents such as sodium borohydride ($NaBH_4$) and stabilizers like Polyvinylpyrrolidone (PVP) yielding ultrasmall Au NPs (average size < 2 nm) shown in Figure 9a. Since gold nanoparticles, especially in the presence of the X-ray beam, easily deposit on the channel walls, the walls were coated such that the channel walls became hydrophobic. This procedure resulted in a significantly reduced deposition of gold. Moreover, the PVP used to stabilize the nanoparticles also decreased the deposition of NPs on the channel walls [46]. The microfluidic device consists of 3 cyclone μ-mixers followed by a microchannel as reactor Figure 9b. The setup is designed to handle high flow rates of reactants in order to achieve a turbulent (Reynolds number above 2300) and plug flow, therefore allowing correlation of beam position and reaction time with high time resolution.

Mapping the oxidation states of gold colloids along the microchannel by XAS with µm spatial and ms time resolution allowed determination of the kinetics of Au NP formation in the first 20 ms of the reaction. The reaction progress was monitored in a continuous rapid flow at different positions along the microchannel by XAS. The measured spectra in Figure 9b-c clearly show a significant contribution of oxidized Au

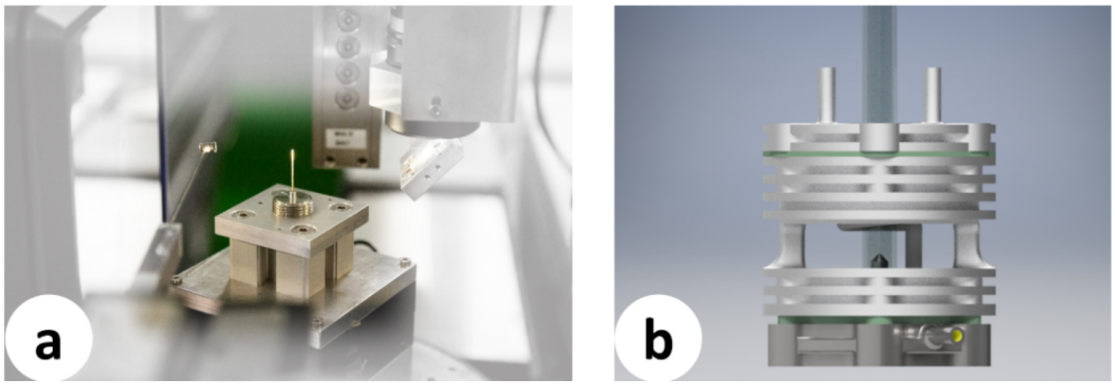

Figure 8: a) Cell body used for the quasi-in situ study of bismuth molybdenum oxides during its application at the P06 beamline at DESY, b) optimized cell body with the possibility for heating in a gas atmosphere during in situ imaging.

after 6 ms, whereas after ca. 10 ms reduction of Au is complete. Therefore, these findings show that the reduction of Au^{3+} by $NaBH_4$ in the presence of PVP proceeds within a fast time frame of 10 ms. Similarly to these metallic gold nanoparticles, the reactor is also used to form bimetallic gold palladium alloys or Cu/ZnO during precipitation reactions. Such spatially resolved studies were already performed for the precipitation of $BaSO_4$, which was carried out in collaboration with Prof. Dr. Dittmeyer and Dr. Kölbl from the Institute for Micro Process Engineering (IMVT) of KIT. Here, the precipitation of $BaSO_4$ derived from $BaCl_2$ and Na_2SO_4 was studied by SAXS at several distances behind the mixer [47], but also the axial profile along the capillary was examined. A significant difference between the suspension close to the capillary walls and the center was observed, which is in correspondence to a different $BaSO_4$ concentration along the axial profile of the capillary, indicating a non-turbulent flow regime and causing different particle sizes and concentrations.

1.10 Multimodal scanning microscopy with diffraction and fluorescence contrast (AG Schroer)

Using the hard x-ray scanning microscope at beamline P06, we have demonstrated three-dimensional multimodal imaging of a microchip test structure from Infineon. The sample was prepared by focused ion beam, creating a small cylinder of approximately 7-8 µm diameter, and raster scanned in tomographic mode, acquiring simultaneously the absorption, the x-ray fluorescence, and the wide-angle x-ray scattering signal of the sample. In this way, the elemental and structural information can be obtained of the sample as a function of three-dimensional position. Fig. 10a) shows the absorption in projection (top) and reconstructed slices at different heights in the microchip marked by 1, 2, and 3. Fig. 10b) shows an exemplary projection in fluorescence for different elements. A reconstructed slice through the tungsten plugs is shown in Fig. 10c). The

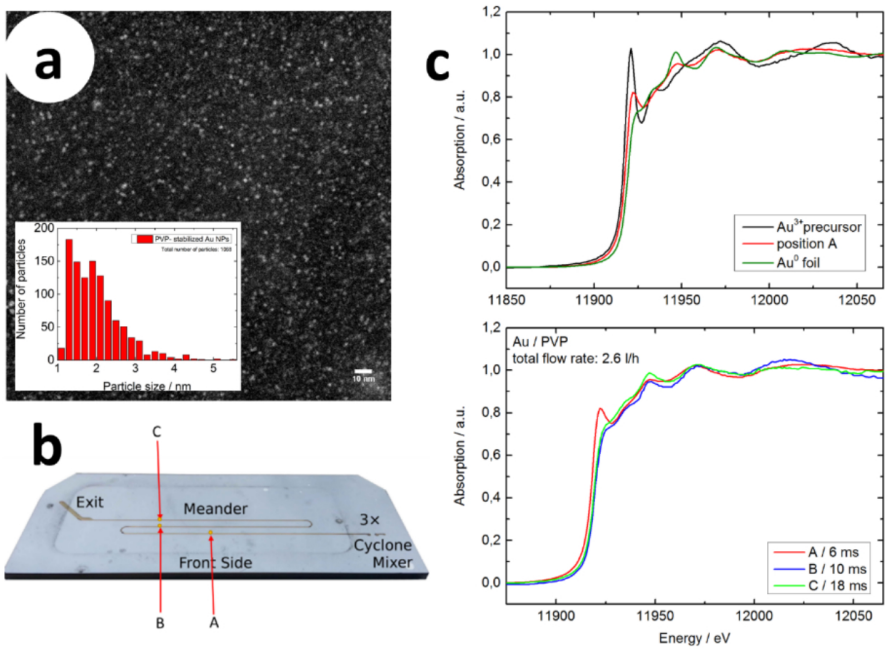

Figure 9: a) TEM image of PVP-stabilized Au NPs synthesized by $NaBH_4$ in the microfluidic reactor, b) microfluidic chip, positions along the channel where in situ XAS was performed are marked by red arrows and c) reference X-ray absorption spectra of Au^{3+} precursor and Au^0 foil compared to absorption data acquired at position A (top) and X-ray absorption near edge structure spectra recorded at different positions correlated to reaction times (bottom).

wide-angle scattering data is extremely rich, containing very finely grained crystalline components, such as thin liner layers, and coarser crystallites in the vias on the scale of the nanobeam (full-width at half maximum beamsize: $\approx 100\,\mathrm{nm}$). Tomographic reconstruction of the data requires different approaches: while isotropic powders can be reconstructed in a straight-forward manner [48], reconstructing the larger crystallites requires the extension of grain mapping schemes [49] to the scanning microscopy case. We have implemented these schemes (milestone Theo5) and are currently applying them to the given data.

1.11 Instrumentation, dissemination of methods and user experiments on in-situ chemical and biological processes (AG Salditt, AG Schroer)

The GINIX nano-focus endstation instrument at beamline P10 at PETRA III was upgraded with a high resolution waveguide stage with better vibration isolation, as well as a high resolution scanning stage. The Eiger X 4M detector was fully integrated in

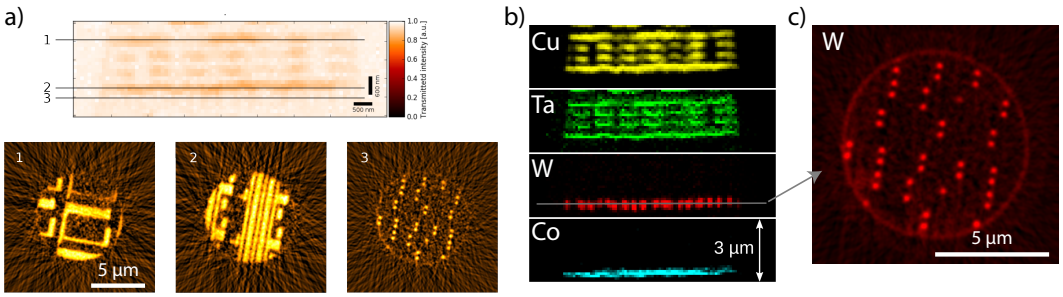

Figure 10: Scanning tomogram of a microchip test structure. a) Absorption tomogram with single projection and three reconstructed slices in different heights. b) Exemplary projection in X-ray fluorescence contrast showing the distribution of different elements. c) Reconstructed slice (tungsten contrast) of the tungsten plug vias [cf. section in b)].

the instrument control. A further emphasis was on fast data acquisition including fast tomography with continuous motor movement and also time-resolved tomography. Few user proposals were granted beamtime, but collaborations with several groups continued, at least concerning data analysis.

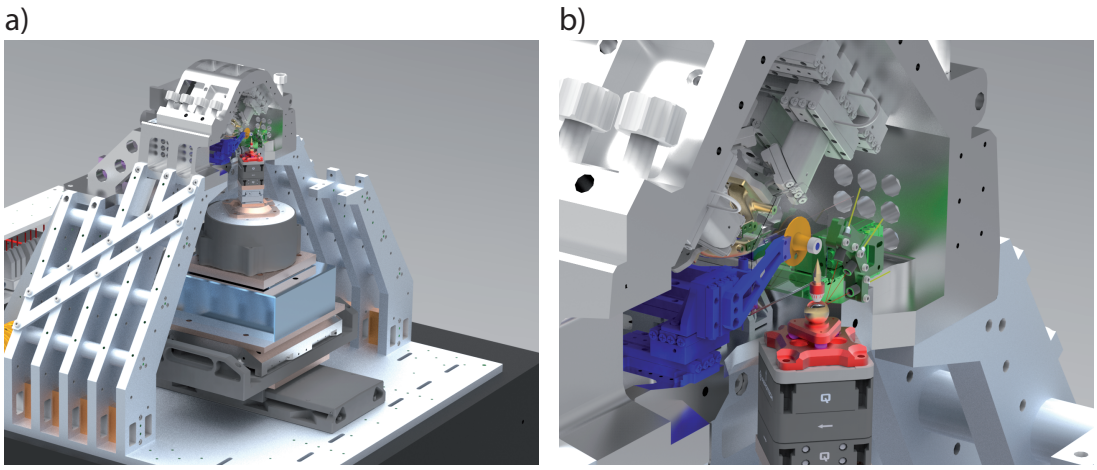

Figure 11: a) Upgraded X-ray scanning microscope at beamline P06. b) Detail of the optics and sample region of the scanner. (red) Sample mount with ball reflector for interferometric position measurements. (green) mount for three laser interferometers, redundantly measuring the position of the sample in the directions transverse to the beam.

The x-ray scanning microscope at P06 was upgraded in 2016 parallel to regular user operation. Fig. 11a) shows the new scanner unit that was designed for stability. Two nanofocusing optics can be aligned in six degrees of freedom, each. The setup can accommodate nanofocusing refractive x-ray optics [50, 51], adiabatically focusing lenses

[52][10], Fresnel zone plates, and multilayer Laue lenses [53]. With a new Eiger X 4M detector, efficient continuous scanning schemes have been implemented, allowing for efficient tomographic ptychography scans. Fig. 12 shows the ptychotomographic

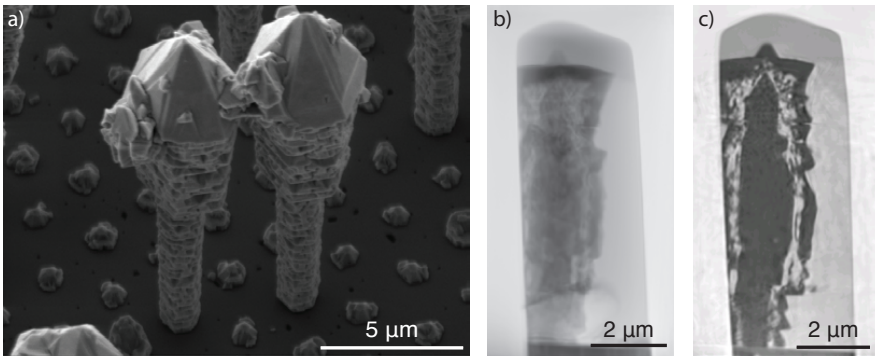

Figure 12: a) SEM image of Ga/GaN nanorods. b) Single ptychographic projection of a single nanorod. c) 2D section through the nanorod after tomographic reconstruction of the 3D dataset.

reconstruction of a Ga/GaN nanorod carried out in collaboration with the group of Michael Hanke from Paul-Drude-Institute in Berlin. A single nanorod was prepared for 3D ptychography at Paul-Drude-Institute [11]. Fig. 12 b) shows a single ptychographic projection of the nanorod and Fig. 12 c) a section through the 3D volume after tomographic reconstruction. 3D ptychography requires a high stability over several hours. The results show that the new scanning microscope has the stability for ptychographic tomography on the level of a few tens of nanometers. Crucial to achieve this stability is the measurement of the relative positions between optical axis and the sample by laser interferometry. Fig. 11b) shows a detail of the scanner unit showing the laser interferometers to measure the sample position (green). The ptychotomogram was recorded in continous scanning mode, recording ptychographic diffraction patterns at a rate of 50 Hz.

2 Erreichte Meilensteine

In the following, we discuss the progress and comment on the individual milestones:

Mfluid5 (year 5) We have now developed a microfluidic platforms, which can be applied (also by beamline users) to a variety of chemical and biological experiments. We are in the process of writing a manuscript in order to make out protocol and bench marking results available to the public. The method has already been used within the VI [3, 12].

Cell 5 (year 5) We have in the meantime conducted scanning SAXS experiments on different cell types and different cellular components (such as the cytoskeleton or

the nucleus) and the Salditt and the Köster group now have advanced the data analysis tools such that cell imaging is now straight forward [4, 5]. We have been invited to write review article for ACS Nano on cell imaging using x-rays.

Mel3 (year 3) Imaging of frozen hydrated melanosomes (milestone reached in 2016).

Alg3 (year 3) Investigation of frozen hydrated marine biofouling organisms and cells (milestone reached in 2016).

Alg4 (year 4) Chemical contrast in adherent marine biofouling organisms (milestone reached in 2016).

Cat5 (year 5) We have progressed towards design and construction of an in situ cell capable of full 3D tomography measurements, and have performed experiments with existing cells through collaboration to provide inspiration for the current design. Several experiments are planned or in progress to address the structure and gradients of catalytic processes in 3D.

React4 (year 4) A microfluidic setup is available for in situ studies of early stage kinetics for nanoparticle synthesis, colloid synthesis, precipitation reactions. First in situ XAS experiments on Au colloid synthesis have been completed, and further studies on precipitation reactions are underway.

Horst5 (year 5) Complete implementation of the liquid jet (milestone reached in 2016).

Theo5 (year 5) Diffraction tomography in SAXS and WAXS regime (milestone reached in 2016).

3 Einhaltung des Finanzierungs- und Zeitplans

The project has ended in March 2017, after a project extension without additional cost due to maternal leaves.

4 Publikationen, Vorträge, Preise etc. bitte gegebenenfalls als Anhang beifügen

4.1 Grants and Awards:

Sarah Köster received an ERC Consolidator Grant for the Project "MECHANICS – Mechanics of cells: the role of intermediate filaments". The aim of the project is to decipher the relation between molecular interactions in filament forming proteins and the mechanical properties of the filaments and eventually of whole cells. This work will build strongly on our previous studies of protein assembly on the nanoscale that was funded by the VI.

The following BMBF projects are building on the results obtained within the VI and are part of the measures to sustain the activities started within the VI:

- "Kryogene Fluotomographie an P06/PETRA III", 05K16PC1 (A. Rosenhahn, et al.)
- "MicTomoCat: Hierarchische in situ röntgenmikroskopische und tomographische Untersuchung von Katalysatoren für die Abgasnachbehandlung und Energiespeicherung", 05K16VK1 (J.-D. Grunwaldt, et al.)

4.2 Meetings & Outreach into the Scientific Community:

A satellite workshop to the DESY Photon Science Users Meeting in Hamburg was organized by the VI-403. It is already the 6th workshop held in the context of the Users Meeting entitled "6th Workshop on X-Ray Nano-Imaging of Biological and Chemical Systems at PETRA III". It aimed at the Photon Science user community interested in nano imaging, giving an overview over the possibilities of nano imaging at the x-ray microscopes at PETRA III (cf. photo below). Users presented their recent results. The workshop was well attended with over 80 participants.

4.3 International Collaborations

Within the activities of the VI the following international collaborations have been established:

- John Miao, UCLA (photoinduced chemical reactions)
- Florian Meirer, Utrecht (tomography of catalytic particles)
- Dimitrov Orlov, Lund (tomography of precipitates in light metals)
- Magdalena Sczerbowska-Boruchowska, Krakov (x-ray microscopy of medical tissues)
- Danielle Pellicia, Melbourne (tomography, fluorescence imaging)
- Jesper Wallentin, Lund (in operando studies of nanowires)
- Ulrich Vogt, KTH Stockholm (x-ray nanooptics)
- Christian Damsgaard, DTU Copenhagen (in-situ cells for imaging catalysts)
- Robert Feidenhansl', Niels Bohr Institute, University of Copenhagen, Copenhagen (Nanowires)
- Advanced Photon Source, Argonne, IL, USA (USAXS on bacteria)
- Shubnikov Institute of Crystallography RAS, Moscow Russia (x-ray physics)
- Van 't Hoff laboratory for Physical and Colloid Chemistry, Debye Institute for Nanomaterials Science, Utrecht University (colloidal systems)
- National Research Nuclear University MEPhI (Moscow Engineering Physics Institute), Moscow, Russia (x-ray physics)
- NRC "Kurchatov Institute", Moscow, Russia (x-ray physics)
- A. Singer, University of California San Diego, La Jolla, California, United States (coherent x-ray imaging techniques)
- National Research Tomsk Polytechnic University (TPU), Tomsk, Russia
- Department of Chemistry and Center for Nanotechnology for Engineering (CNIS), University of Rome Sapienza, Rome, Italy
- Landau Institute for Theoretical Physics, Russian Academy of Sciences, Chernogolovka, Russia
- Moscow Institute of Physics and Technology (State University), Dolgoprudny, Russia
- Skobeltsyn Institute of Nuclear Physics, Lomonosov Moscow State University, Moscow, Russia
- NanoLund, Department of Physics, Lund University, Lund, Sweden
- Diamond Light Source, UK (in situ chemical imaging in catalysis)
- Michael Hanke, Paul-Drude-Institute, Berlin (3D ptychography of core-shell nanorods).

4.4 Outreach

- C. G. Schroer, "Spatially-Resolved Materials Characterization with Synchrotron Radiation", EMU School, Vienna, Austria, Sept. 20, 2016
- S. Köster, "X-Ray Microscopy", Bad Honnef Summer School on "Advanced Microscopy – Physical Concepts and Impacts in Life Sciences", June 2017

Publications in the Reporting Period

[1] J.-D. Nicolas, M. Bernhardt, M. Krenkel, C. Richter, S. Luther, and T. Salditt, J. Appl. Cryst. **50**, 612 (2017).

[2] M. Bernhardt, J. D. Nicolas, M. Eckermann, B. Eltzner, F. Rehfeldt, and T. Salditt, New J. Phys. **19**, 013012 (2017).

[3] O. Saldanha, R. Graceffa, C. Y. J. Hémonnot, C. Ranke, G. Brehm, M. Liebi, B. Marmiroli, B. Weinhausen, M. Burghammer, and S. Köster, Chem. Phys. Chem. (2017), DOI: 10.1002/cphc.201700221.

[4] C. Y. J. Hémonnot, C. Ranke, O. Saldanha, R. Graceffa, J. Hagemann, and S. Köster, ACS Nano **10**, (2016).

[5] C. Y. J. Hémonnot, J. Reinhardt, O. Saldanha, J. Patommel, R. Graceffa, B. Weinhausen, M. Burghammer, C. G. Schroer, and S. Köster, ACS Nano **10**, 3553 (2016).

[6] S. Baier, C. D. Damsgaard, M. Scholz, F. Benzi, A. Rochet, R. Hoppe, T. Scherer, J. Shi, A. Wittstock, B. Weinhausen, J. B. Wagner, C. G. Schroer, and J.-D. Grunwaldt, Microscopy and Microanalysis **22**, 178 (2016).

[7] S. Baier, A. Wittstock, C. D. Damsgaard, A. Diaz, J. Reinhardt, F. Benzi, J. Shi, T. Scherer, D. Wang, C. Kübel, C. G. Schroer, and J.-D. Grunwaldt, RSC Adv. **6**, 83031 (2016).

[8] S. Baier, C. D. Damsgaard, M. Klumpp, Z. Balogh, J. Reinhardt, T. Kasama, T. Sheppard, F. Benzi, J. B. Wagner, W. Schwieger, C. G. Schroer, and J.-D. Grunwaldt, Microscopy and Microanalysis (2017), DOI: 10.1017/S1431927617000332.

[9] G. Hofmann, G. Tofighi, G. Rinke, S. Baier, A. Ewinger, A. Urlab, A. Wenka, S. Heideker, A. Jahn, R. Dittmeyer, and J.-D. Grunwaldt, J. Phys. Conf. Ser. **712**, 012072 (2016).

[10] J. Patommel, S. Klare, R. Hoppe, S. Ritter, D. Samberg, F. Wittwer, A. Jahn, K. Richter, C. Wenzel, J. W. Bartha, M. Scholz, F. Seiboth, U. Boesenberg, G. Falkenberg, and C. G. Schroer, Appl. Phys. Lett. **110**, 101103 (2017).

[11] T. Krause, M. Hanke, L. Nicolai, Z. Cheng, M. Niehle, A. Trampert, M. Kahnt, G. Falkenberg, C. G. Schroer, J. Hartmann, H. Zhou, H.-H. Wehmann, and A. Waag, Phys. Rev. Applied **7**, 024033 (2017).

[12] O. Saldanha, M. E. Brennich, M. Burghammer, H. Herrmann, and S. Köster, Biomicrofluidics **10**, 024108 (2016).

[13] J. Hagemann, A.-L. Robisch, M. Osterhoff, and T. Salditt, J. Synchrotron Rad. **24**, 498 (2017).

[14] T. Jahn, R. N. Wilke, Y. Chushkin, and T. Salditt, Acta Cryst. A **73**, 1 (2017).

[15] A. Ruhlandt and T. Salditt, Acta Cryst. A **72**, 1 (2016).

[16] J. Wallentin, M. Osterhoff, and T. Salditt, Adv. Mater. **28**, 1788 (2016).

[17] M. Bernhardt, M. Priebe, M. Osterhoff, C. Wollnik, A. Diaz, T. Salditt, and F. Rehfeldt, Biophys. J. **110**, 680 (2016).

[18] S. Hoffmann-Urlaub, P. Höhne, M. Kanbach, and T. Salditt, Microelectronic Engineering **164**, 135 (2016).

[19] S. Hoffmann-Urlaub and T. Salditt, Acta Cryst. A **72**, 515 (2016).

[20] M. Töpperwien, M. Krenkel, K. Müller, and T. Salditt, Proc. SPIE **9967**, 99670T (2016).

[21] T. Salditt and S. Aeffner, Seminars in Cell & Developmental Biology **60**, 65 (2016).

[22] A. D. Surowka, M. Töpperwien, M. Bernhardt, J. D. Nicolas, M. Osterhoff, T. Salditt, D. Adamek, and M. Szczerbowska-Boruchowska, Talanta **161**, 368 (2016).

[23] A.-L. Robisch, J. Wallentin, A. Pacureanu, P. Cloetens, and T. Salditt, Opt. Lett. **41**, 5519 (2016).

[24] A. R. von Gundlach, V. M. Garamus, T. M. Willey, J. Ilavsky, K. Hilpert, and A. Rosenhahn, J. Appl. Cryst. **49**, 2210 (2016).

[25] T. Senkbeil, T. Mohamed, R. Simon, D. Batchelor, A. Di Fino, N. Aldred, A. S. Clare, and A. Rosenhahn, Anal. Bioanal. Chem. **408**, 1487 (2016).

[26] A. R. von Gundlach, V. M. Garamus, T. Gorniak, H. A. Davies, M. Reischl, R. Mikut, K. Hilpert, and A. Rosenhahn, Biochimica et Biophysica Acta (BBA) - Biomembranes **1858**, 918 (2016).

[27] C. G. Lopez, O. Saldanha, K. Huber, and S. Köster, Proc. Natl. Acad. Sci. USA **113**, 11152 (2016).

[28] D. Dzhigaev, A. Shabalin, T. Stankevic, U. Lorenz, R. P. Kurta, F. Seiboth, J. Wallentin, A. Singer, S. Lazarev, O. M. Yefanov, M. Borgström, M. N. Strikhanov, L. Samuelson, G. Falkenberg, C. G. Schroer, A. Mikkelsen, R. Feidenhans'l, and I. A. Vartanyants, J. Opt. **18**, 064007 (2016).

[29] O. Y. Gorobtsov and I. A. Vartanyants, Phys. Rev. B **93**, 184107 (2016).

[30] I. A. Zaluzhnyy, R. P. Kurta, A. P. Menushenkov, B. I. Ostrovskii, and I. A. Vartanyants, Phys. Rev. E **94**, 030701(R) (2016).

[31] R. P. Kurta, M. Altarelli, and I. A. Vartanyants, Advances in Chemical Physics **161**, 1 (2016).

[32] A. G. Shabalin, J.-M. Meijer, R. Dronyak, O. M. Yefanov, A. Singer, R. P. Kurta, U. Lorenz, O. Y. Gorobtsov, D. Dzhigaev, S. Kalbfleisch, J. Gulden, A. V. Zozulya, M. Sprung, A. V. Petukhov, and I. A. Vartanyants, Phys. Rev. Lett. **117**, 138002 (2016).

[33] J. Reinhardt, R. Hoppe, G. Hofmann, C. D. Damsgaard, J. Patommel, C. Baumbach, S. Baier, A. Rochet, J.-D. Grunwaldt, G. Falkenberg, and C. G. Schroer, Ultramicroscopy **173**, 52 (2017).

[34] C. G. Schroer, C. Baumbach, R. Döhrmann, S. Klare, R. Hoppe, M. Kahnt, J. Patommel, J. Reinhardt, S. Ritter, D. Samberg, M. Scholz, A. Schropp, F. Seiboth, M. Seyrich, F. Wittwer, and G. Falkenberg, AIP Conference Proceedings **1741**, 030007 (2016).

References

[35] P. A. Riley, Pigm. Cell Res. **16**, 548 (2003).

[36] J. Reinhard, S. Wiemann, S. Joachim, H. Schmid, B. Denecke, Y. Wang, G. Downey, and A. Faissner, IOVS **54**, 6223 (2013).

[37] S. Ito, P. Natl. Acad. Sci. USA **103**, 14647 (2006).

[38] T. Gorniak, T. Haraszti, H. Suhonen, Y. Yang, A. Hedberg-Buenz, D. Koehn, R. Heine, M. Grunze, A. Rosenhahn, and M. G. Anderson, Pigment Cell & Melanoma Research **27**, 831 (2014).

[39] A. Chiovitti, P. Heraud, T. M. Dugdale, O. M. Hodson, R. C. A. Curtain, R. R. Dagastine, B. R. Wood, and R. Wetherbee, Soft Matter **4**, 811 (2008).

[40] R. Holland, T. M. Dugdale, R. Wetherbee, A. B. Brennan, J. A. Finlay, J. A. Callow, and M. E. Callow, Biofouling **20**, 323 (2004).

[41] J.-D. Grunwaldt and B. S. Clausen, Topics Catal. **18**, 37 (2002).

[42] B. Bems, R. Schlögl, and T. Ressler, J. Synchrotron Rad. **8**, 619 (2001).

[43] J. B. Hansen and P. E. Højlund Nielsen, *Handbook of Heterogeneous Catslysis* (PUBLISHER, ADDRESS, 2008).

[44] M. Rahman and E. Rebrov, Processes **2**, 466 (2014).

[45] J. Wagner and J. M. Köhler, Nano Lett. **5**, 685 (2005).

[46] H. Tsunoyama, N. Ichikuni, and T. Tsukuda, Langmuir **24**, 11327 (2008).

[47] A. Kölbl, M. Kraut, and A. Wenka, Chem. Eng. J. **167**, 444 (2011).

[48] P. Bleuet, E. Welcomme, E. Dooryhée, J. Susini, J.-L. Hodeau, and P. Walter, Nature Materials **7**, 468 (2008).

[49] G. Johnson, A. King, M. G. Honnicke, J. Marrow, and W. Ludwig, Journal of Applied Crystallography **41**, 310 (2008).

[50] C. G. Schroer, M. Kuhlmann, U. T. Hunger, T. F. Günzler, O. Kurapova, S. Feste, F. Frehse, B. Lengeler, M. Drakopoulos, A. Somogyi, A. S. Simionovici, A. Snigirev, I. Snigireva, C. Schug, and W. H. Schröder, Appl. Phys. Lett. **82**, 1485 (2003).

[51] C. G. Schroer, O. Kurapova, J. Patommel, P. Boye, J. Feldkamp, B. Lengeler, M. Burghammer, C. Riekel, L. Vincze, A. van der Hart, and M. Küchler, Appl. Phys. Lett. **87**, 124103 (2005).

[52] C. G. Schroer and B. Lengeler, Phys. Rev. Lett. **94**, 054802 (2005).

[53] A. Kubec, S. Braun, S. Niese, P. Krüger, J. Patommel, M. Hecker, A. Leson, and C. G. Schroer, J. Synchrotron Rad. **21**, 1122 (2014).